Hydrogen-Induced Restructuring of a Cu(100) Electrode in Electroreduction Conditions

Zisheng Zhang,[a] Ziyang Wei,[a] Philippe Sautet,[a,b,c,*] Anastassia N. Alexandrova[a,c,*]

[a] Department of Chemistry and Biochemistry, [b] Department of Chemical and Biomolecular Engineering, and [c] California NanoSystems Institute, University of California, Los Angeles, CA 90094, USA

ABSTRACT

The rearrangement of Cu surfaces under electrochemical conditions has been demonstrated to play a key role in the surface activation for major electrocatalytic reactions. Despite the extensive experimental insights from surface-sensitive spectroscopic and microscopic methods, their spatial and temporal resolution are far from ideal. Theoretical investigations have also been challenged by the diversity of restructuring configurations, surface stoichiometry, adsorbate configurations, and the effect of electrode potential. Here, we tackle this complexity of the electrochemical interface by grand canonical DFT and global optimization techniques, which explore the chemical space of Cu(100) restructuring with varying applied potential and adsorbate coverage from first principles. We show that electroreduction conditions cause the formation of a shifted-row reconstruction on Cu(100), induced by hydrogen adsorption. The simulated STM images of the calculated reconstructed structures agree with experimental *in situ* STM images, which validates our results. The found shifted-row reconstruction is initiated and stabilized 1/6 ML H coverage since this weakens the Cu-Cu bonds between top- and sub-layer and at 1/3 ML fills all the created 3-fold hollow sites with H adsorbates. Different statistical models are used to study the potential- and pH-dependence of the surface stability diagram. The kinetics and dynamics of surface atoms are studied with BOMD simulations, and their dependence on H coverage and initial configuration is discussed. This manuscript provides rich insight into surface restructuring in electroreduction conditions, which is required for the understanding and rational design of Cu-based materials for electrocatalytic processes and beyond.

INTRODUCTION

Understanding of the surface structure is crucial for investigation of catalytic/deactivation mechanisms and for further optimization of the heterogeneous catalyst. However, the conventional static bulk-derived surface slab is often insufficient for representing the realistic catalytic interface. Under reaction conditions, the catalyst surface is in constant adsorbate exchange with its environment and may be subject to electrochemical potential or near-surface electrolyte polarization – such factors can induce nontrivial structural rearrangement, dynamical behavior, or populating an ensemble of coexisting metastable surface states with diverse structures and reactivities.[1,2] Even the simplest adsorbate, H, can induce dramatic restructuring on various metal surfaces.[3]

Cu has been the only transition metal that can catalyze CO_2 reduction reaction (CO_2RR) efficiently towards deeper C_{2+} reduction products beyond CO.[4] Such reactivity, as well as the low cost and earth-abundance of Cu, has made Cu-based materials a research hot spot in the energy and environmental science in the recent decade.[5,6] However, with the development of electrochemical *in situ* characterization techniques, the Cu-based catalysts has been probed to undergo dramatic restructuring under electrochemical conditions, including surface phase transitions,[7] reversible morphological change in nanoscale,[8,9] potential- and CO- induced nanoclustering,[10,11] nanocrystal reconstruction,[12] and undercoordinated Cu structure formation[13].

One of the most intriguing types of restructuring is the formation of stripes on Cu(100) observed via *in situ* STM during hydrogen evolution reaction (HER), one of the most studied electrocatalytic reactions, more specifically in acidic media ($HClO_4$, pH=1) at reducing potential of -0.326 V_{SHE}.[14] The stripes become sharper at -0.396 V_{SHE}, showing that they consist of two atomic rows. As the potential sweeps to -0.406 V_{SHE}, neighboring stripes start to form, which roughly doubles the surface concentration of stripes. The inter-stripe regions (forming a dark line) becomes darker at -0.436 V_{SHE} with tiny periodic bright spots along the dark stripe.[15] Such stripe formation is hindered at higher pH, with the onset potential of stripe formation first shifted to a more negative potential (-0.456 V_{SHE} at pH=2 and -0.586 V_{SHE} at pH=2.75), and the stripes becoming blurrier. Beyond pH=3, no restructuring is observed.[14] The observed reconstruction results in a an increase of the electrode reactivity for HER. Although several surface structures of the stripes have been proposed,[14,16] they are either putative or based on small unit cell simulations. In addition, the diversity of adsorbate configurations/coverages and the potential-/pH-dependence, which have been shown to be necessary for describing electrochemical interfaces,[17] are not well addressed using static model and constant-charge DFT.

Here we interrogate the atomic mechanism of hydrogen-induced restructuring of Cu(100) under electrocatalytic reduction potential. The chemical space of surface reconstruction, adsorbate coverage, and adsorption sites is efficiently sampled by grand canonical genetic algorithm (GCGA) global optimization to construct an ensemble of structurally diverse and chemically relevant surface configurations under different hydrogen coverages. Potential dependence of the surface states are investigated by grand canonical DFT (GCDFT), and a row-shifting reconstruction is found to emerge upon hydrogen coverage and negative potentials. Surface stability diagrams as a function of electrode potential and pH are investigated using different statistical models, and corrections that can be made to the purely thermodynamics picture of the system are discussed. The electronic structure origin of the restructuring is rationalized with a chemical bonding analysis, revealing the key role for hydrogen adsorption of the formed 3-fold hollow sites upon the row-shifting process. The coverage-dependence of the various surface events are probed with Born-Oppenheimer molecular dynamics and transition state search. This study provides insights into the energetics, dynamics, and chemical bonding of the electrochemical potential and hydrogen coverage induced restructuring of Cu(100) surface, which can advance our understanding of the electrocatalytic interface and guide the design of active and durable electrocatalysts.

RESULTS & DISCUSSION

Due to the vast chemical space spanned by the configurational and compositional degrees of freedom, the grand canonical genetic algorithm (GCGA)[18,19] is used to globally optimize the geometry and stoichiometry of the 4-layer 6×6 supercell of Cu(100) under coverage of H (simulation cell and algorithm flow chart are in Figure S1). Specifically, the system is allowed to exchange H with a reservoir with a fixed H chemical potential, $\mu_{\mathrm{H}}(\mathrm{pH}, U, T)$. To cover the chemically relevant range of μ_{H}, eight GCGA searches are performed at pH of 1 and electrode potential of 0 V_{SHE}, -0.15 V_{SHE}, -0.2 V_{SHE}, -0.25 V_{SHE}, -0.3 V_{SHE}, -0.4 V_{SHE}, -0.5 V_{SHE}, and -0.75 V_{SHE}.

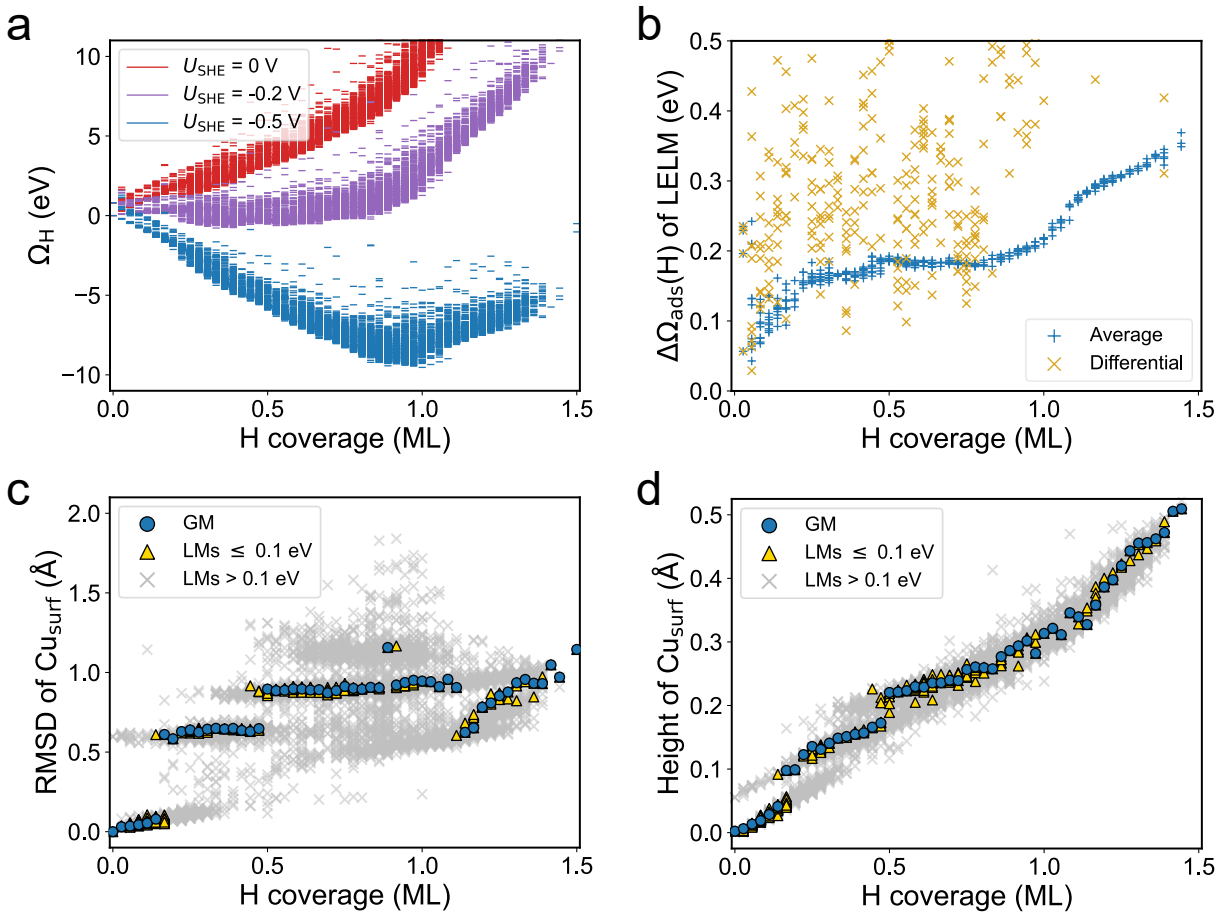

Figure 1. Energetic and geometric analysis of the surface states from GCGA sampling. (a) The grand canonical free energy as a function of H coverage at different potentials, (b) Average and differential (with respect to the GM of the pre-adsorption coverage) adsorption free energy plotted versus H coverage at pH=1 and U_{SHE}=0 V. (c) The RMSD of surface Cu coordinate with respect to the pristine Cu(100), (d) average height of surface Cu for the GM, low-energy local minima, and other minima, plotted versus H coverage.

In total, 7420 unique surface states are obtained in a rather broad stoichiometric distribution (Figure S2), with H coverage ranging from 0H to 54H per supercell (θ_H from 0 to 1.5 ML). There are multiple low-energy local minima (LMs) surface states within 0.1 eV (corresponding to a Boltzmann factor of 1/49 at 298.15 K) from the global minimum (GM) of each stoichiometry (Figure S2), suggesting coexisting surfaces states at room temperature. Hence, we treat the obtained surface states (of diverse surface configurations) in a grand canonical ensemble of adsorbates and compute their grand canonical free energy Ω_H as a function of μ_H. At 0 V_{SHE}, Ω_H increases with H coverage, suggesting unfavorable H adsorption (Figure 1a). At more negative potentials, the μ_H increases, favoring the higher coverage surface states. The shape of the free energy plot (Figure 1a) resembles a

convex hull; however, it is not as continuous. The average ΔG_H of surface states exhibits "jumps" at c.a. 1/6 ML, 1/3 ML, 2/3 ML, and 1 ML H coverage (Figure 1b). In fact, the curve seems to consist of several local convex hulls, possibly due to each corresponding to different local bonding patterns, and the transition region between them gives rise to the jump in ΔG_H.

To understand the cause of such unusual energetics, we analyze the geometry of the surface states, with a focus on the GMs and LMs of each coverage. The RMSD of the top-layer Cu (referenced to the unrestructured bare surface) are shown in Figure 1c. Below 1/6 ML coverage, the RMSD of the GMs and LMs stays below 0.1 Å, showing no significant structural change of the copper. At 1/6 ML coverage, the RMSD jumps to c.a. 0.6 Å, marking the first stage of the restructuring. This corresponds to the shift of one atomic row on the Cu surface by half a Cu-Cu distance, creating a double-row of 3-fold Cu hollow site to maximize adsorbate binding (Figure 2). At 1/2 ML coverage, the RMSD jumps to c.a. 0.9 Å, which is attributed to a second shifted row in the unit cell, so that out of every three rows one is shifted. This resembles the surface oxide configurations.[20] Each row-shifting is accompanied by an increase in the height of top-layer Cu atoms due to elevation of the shifted row (Figure 1d). This surface Cu configuration remains until 10/9 ML H where the RMSD of Cu_{surf} goes back to c.a. 0.6 Å and then keeps increasing as coverage increases. This corresponds to the filling of sub-surface sites by H, causing continuous structural change (Figure S3). At c.a. 4/3 ML coverage, a third shifted row occurs, and the surface is transformed into an elongated (111)-like configuration, with a H-saturated top-surface and a significant concentration of sub-surface H.

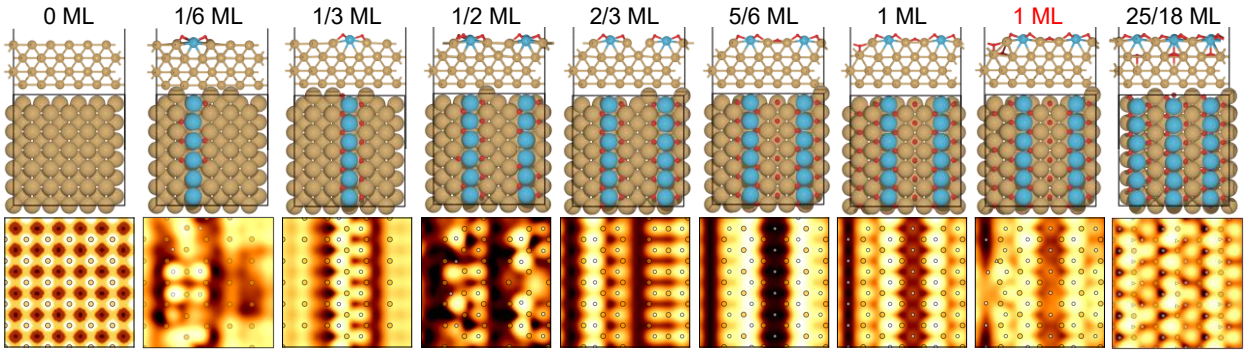

Figure 2. Geometries and simulated STM images of the key surface states. The side view, top view, and simulated STM images of the GM surface state of key coverage cases. The shifted atomic rows and surface H are highlighted by blue and red, respectively. The second to last column shows the restructured surface at 1 ML H coverage including a sub-surface H (*vide infra*).

To link the found surface structures with the experimental STM images,[14,15] STM simulations based on geometries of selected GMs and LMSs are performed (Figure 2 and

Figure S4). A very distinct image contrast is shown as a function of H coverage/Cu restructuring explaining the changes seen in the experiment. The current on Cu atoms close to H adsorbates is generally decreased, since this interaction shifted some Cu states away from the Fermi level, while H atoms at highest z coordinate themselves appear as new protrusions. At 1/6 ML, the shifted row has formed, but the induced 3-fold hollow sites are only partially filled, leading to a disordered pattern. At room temperature, thermal fluctuation enable H migration along the shifted rows (*vide infra*), and that can yield a more ordered image since STM measures time-average on the time-scale of milliseconds per pixel. Experiments notes a "blurry stripe" potential regime (-0.326 V_{SHE}) which corresponds to this low coverage situation.[15] At 1/3 ML coverage, the shifted Cu row is fully coordinated by H, suppressing the H migration along it and giving a well-defined bright stripe in the image, in agreement with experiment at potential -0.396 V_{SHE}. The second row-shifting initiates at the 1/2 ML coverage and the row is saturated at 2/3 ML, corresponding to the potential regime (-0.406 V_{SHE}) where neighboring stripes start to form. The formation of parallel stripes is due to the frustration in the lattice caused by the initial row-shifting, which acts similarly to a nucleation site in crystal growth. Next, H start to fill the inter-stripe region. Since the shifted row draws neighboring rows closer to it, the Cu-Cu distance of the inter-stripe regions are elongated, and H atoms have a low z coordinate, resulting in a decrease of the neighboring Cu contribution to the image with no bright features from H. A darker region in the image therefore develops in-between the stripes, as seen in the experiment at (-0.436 V_{SHE}). Subsurface H atoms can be populated at coverage $>$ 1 ML and they induce an upward relaxation of surface Cu atoms above them, and bright spots in the inter-stripe regions seen also in the experiment (see supplementary Note 3 and associated Figures). Beyond the coverage of 10/9 ML, the surface restructures into an elongated (111)-like configuration with the surface layer deeply hydrogenated. Although such phase is a thermodynamic minimum, we expect it to be unfeasible and metastable with respect to (i) competing hydrogen evolution reaction (HER) at very negative potential, and (ii) the decomposition of surface hydride to form H_2 in acidic media.[21] Some other notable reported structures and motifs are discussed in Supplementary Note 6-7.

The electronic origin of the row-shifting restructuring is addressed in Figure 3. At the unrestructured bare Cu(100), the Cu_{top} has a slightly negative Bader charge (Figures 3a, S3), and it transfers electrons to H_{ads} upon adsorption. At high H coverages, the charge on Cu_{top} converges at c.a. +0.30 |e|, which is quite close to that in CuH (+0.38 |e|). The charge on H_{ads} stays around -0.30 |e| at all coverages, even upon row-shifting, and in the entire potential window (Figure S4). The change in surface bonding reveals deeper details. Electron localization function (ELF) are plotted for unrestructured bare Cu(100),

unrestructured surface at 1/3 ML coverage, and shifted-row surface with 1/3 ML coverage (Figure 3b). The analysis suggests that, upon H adsorption, Cu-H bonds form, and the Cu_{top}-Cu_{sub} bonds vanish, explaining why the shifted-row configuration is thermodynamically favorable only at higher H coverage. Upon row-shifting, the Cu in the shifted row (Cu_{shf}) and in the neighboring rows (Cu_{nbr}) are further elevated by 0.428 and 0.162 Å, compared to the unrestructured structure. The ELF lobe corresponding to Cu-H are enlarged, suggesting strengthening of the Cu-H bond. The ELF lobe in the Cu_{nbr}-Cu_{sub} are also enlarged slightly, attracting Cu_{nbr} toward Cu_{shf} by 0.246 Å. The weakening of the Cu_{top}-Cu_{sub} by H_{ads} can be shown more clearly in the color-filled contour map of ELF cross section in Figure 3c.

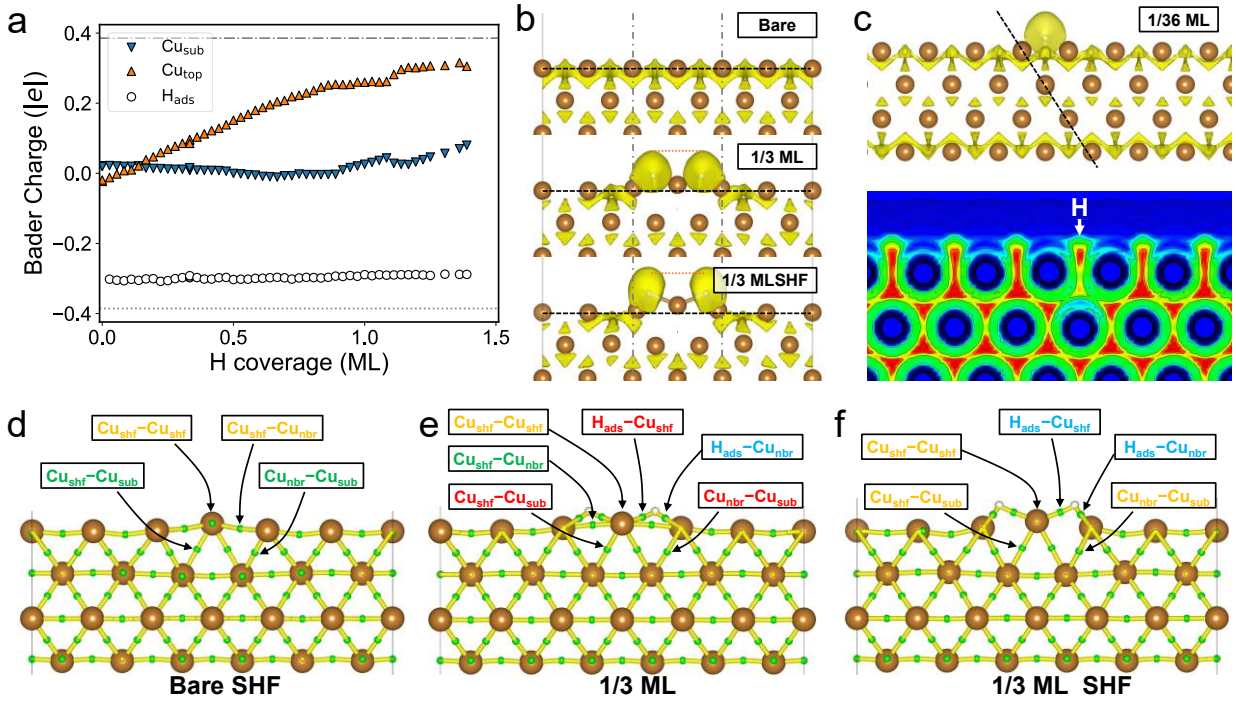

Figure 3. Electronic structure and chemical bonding analysis of the H-covered Cu(100). (a) Average Bader charge of the top-layer, sub-layer, and H adsorbates of the global minimum surface state of each coverage, respectively. (b) ELF isosurfaces of the bare Cu(100), unrestructured Cu(100) at 1/3 ML coverage, and shifted-row Cu(100) at 1/3 ML coverage at isovalue of 0.275. (c) Color-filled contour map of the ELF cross-section of Cu(100) with 1 H showing weakening of Cu-Cu bond between top-layer and sub-layer. The bond critical points and bond paths for (d) shifted-row bare Cu(100), (e) unrestructured Cu(100) at 1/3 ML coverage, and (f) shifted-row Cu(100) at 1/3 ML coverage, with key bonds labeled. Labels are colored according to their ρ_{BCP} relative to surface Cu-Cu in unrestructured bare Cu(100) or Cu-H in 1H-covered Cu(100) with color code: red (lower than reference by more than 0.005), yellow (lower than reference by less than 0.005), green (higher than reference by less than 0.005), and blue (higher than reference by more than 0.005).

To quantify the found bonding changes, quantum theory of atom in molecule (QTAIM) analysis is performed (Figure 3d-f, Table 1), where the charge density at bond critical points, BCPs, (ρ_{BCP}) is used as a bond-strength descriptor. If the Cu row is shifted in the absence of surface H, the Cu_{shf}-Cu_{sub} and Cu_{nbr}-Cu_{sub} would be strengthened slightly. However, the Cu_{shf}-Cu_{nbr} is significantly weakened, which destabilizes the shifted row. When the Cu row is saturated by H at 1/3 ML, the Cu_{shf}-Cu_{sub} and Cu_{nbr}-Cu_{sub} are further weakened. Meanwhile, the H_{ads}-Cu_{shf} and H_{ads}-Cu_{nbr} are of a similar strength as that of H-Cu at 1H coverage. However, when the H-saturated Cu row shifts, the strengths of Cu_{shf}-Cu_{sub} and Cu_{nbr}-Cu_{sub} is restored, which is close to the strength of Cu_{top}-Cu_{sub} in the base unrestructured case. At the same time, the binding site of H switches from 4-fold to 3-fold hollow, boosting the strength of H_{ads}-Cu_{shf} and H_{ads}-Cu_{nbr} to a similar extent as Cu-H in CuH. The above results are further supported by crystal orbital Hamilton population analysis (key data shown in Table 1, and details in Figures S5-10). In summary, the H adsorbates can greatly stabilize the shifted row by filling the 3-fold hollow sites in a hydride-like bonding mode.

Table 1. Quantum Theory of Atoms in Molecules (QTAIM) and Crystal Orbital Hamilton Population (COHP) analysis of different types of chemical bonds. In each cell, the charge density at bond critical point ρ_{BCP} (as the first entry) and the integrated COHP (-ICOHP) up to E_{F} (in parenthesis) are provided. A few reference values: Cu-Cu in bulk Cu: 0.0392 (0.314); Cu-H in bulk CuH: 0.0700 (0.814).

	Bare	Bare shifted-row	1/36 ML	1/3 ML	1/3 ML shifted-row
$Cu_{top}-Cu_{top}$	0.039 (0.23)	-	0.041 (0.26)	-	-
$Cu_{top}-Cu_{sub}$	0.039 (0.23)	-	0.033 (0.15)	-	-
$Cu_{shf}-Cu_{shf}$	-	0.038 (0.34)	-	0.038 (0.31)	0.035 (0.26)
$Cu_{shf}-Cu_{nbr}$	-	0.033 (0.20)	-	0.042 (0.24)	- (0.10)
$Cu_{shf}-Cu_{sub}$	-	0.040 (0.28)	-	0.027 (0.18)	0.035 (0.26)
$Cu_{nbr}-Cu_{sub}$	-	0.039 (0.25)	-	0.033 (0.16)	0.036 (0.21)
$H_{ads}-Cu_{shf}$	-	-	0.055 (0.46)	0.049 (0.46)	0.072 (0.89)
$H_{ads}-Cu_{nbr}$	-	-	-	0.062 (0.48)	0.073 (0.60)

We now investigate how the surface phase evolves at different pH and electrode potential. To obtain the exact potential-dependent electronic free energy Ω_{el} of the surface, we refined all LMs within 0.25 eV from the GM of their coverage with grand canonical DFT, using the surface charging technique with a polarizable continuum solvation model.[22] In this way, we can calculate the total free energy Ω_{tot} of each surface state in the grand canonical ensemble of electrons and adsorbates at different pH and electrode potential. If

we assume that the surface is representable by a single state with the lowest Ω_{tot}, GM, at pH=1 and within the potential window of 0 to -0.5 V_{SHE}, the coverages of 1/6 ML (first Cu row-shifting), 5/6 ML (second row-shifting), and 1 ML (filling of inter-stripe region by H) are predicted to form at -0.11, -0.20, and -0.44 V_{SHE}, respectively. If we approximate the population distribution of all accessible LMs by Boltzmann statistics, the steps would be smoothened but the major coverage stages are still the same. The Pourbaix diagram of surface phases as a function of pH and electrode potential is shown in Figure 4a. As pH increases, the phase boundaries corresponding to coverage increase (accompanied by restructuring) shift to more negative potentials, and that is qualitatively consistent with the postponed potential onset of restructuring at higher pH in ref [14]. However, the predicted potentials corresponding to row-shifting deviate from the experiment by up to 300 mV. The non-linear shift of onset potential at pH beyond 2.75 is also not reflected in the thermodynamic picture. Moreover, it is questionable whether the predicted coverage jump from 1/6 ML to 5/6 ML is kinetically feasible.

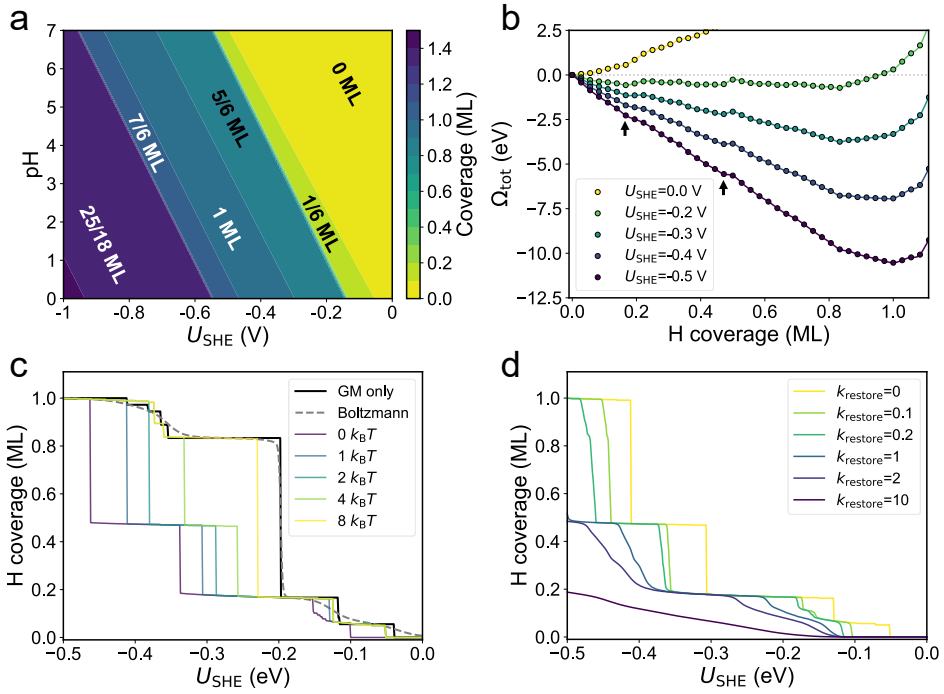

Figure 4. Potential- and pH-dependence of the Cu surface state. (a) Surface Pourbaix diagram assuming global thermodynamic equilibrium, the color bar indicating the H coverage (in ML). (b) Total grand canonical free energy (adsorbates and electrons) as a function of H coverage at different electrode potentials. Metastable local minima are marked by black arrows. (c) Evolution of H coverage during a simulated cathodic scan within a GM-only picture and a Boltzmann picture at global thermodynamic equilibrium, and test cases with different thermal energy supplied to the system considering the metastable states. (d) Evolution of H coverage during a simulated cathodic

scan with different restoring force constant (in units of eV per adsorbate^2) and thermal energy of 1 $k_B T$.

Hence, here we view the restructuring-coupled coverage increase as a reaction coordinate and inspect the free energy change during this process. In Figure 4b, the ensemble-averaged Ω_{tot} is plotted as a function of H coverage at different potentials. During a cathodic scan, the initial state of the surface is clean (zero coverage) at 0 V_{SHE}. At -0.2 V_{SHE}, the higher coverages of up to 17/18 ML become more stable than the clean surface, and several coverages become competitive: 1/6 ML, 1/3 ML, 1/2 ML, and 5/6 ML. However, not all of them appear to be readily kinetically accessible from the initial state: coverage increase encounters several local maxima in free energy. To be specific, the row-shifting is initiated at partial coverage, where the 3-fold hollow sites formed along the stripe bind H more strongly than the unrestructured regions. This causes the system to switch to another free energy surface, which is overall deeper and has its minimum at a higher coverage. The crossing of the two surfaces (the unrestructured and the shifted- row reconstruction) leads to a "spike" on the restructuring-coverage coupled surface in Figure 4b. Hence, the free energy landscape should be treated as a multi-well model with "coverage barriers" separating the minima. At more negative potentials, although the higher 5/6 ML coverage suddenly becomes the GM, there are still kinetic barriers to reach 5/6 ML via intermediate coverages through adsorption or desorption. Hence, the system is likely to be trapped in a metastable state with intermediate coverage, until more negative potential reshapes the free energy surface and smoothens the barriers (Schematic S1). This scenario is analogous to the formation of metastable domains in phase transition dynamics.[23]

We can describe the surface restructuring during the cathodic scan by modeling the system as a particle in a one-dimension multi-minima free energy potential, with the H coverage as the reaction coordinate. As the electrode potential scans from 0 to -0.5 V_{SHE}, the free energy landscape is reshaped, and the new coordinate of the system is determined by a local optimization. From thermal fluctuations, the system is allowed to access neighboring coverages or cross coverage barriers when applicable. In Figure 4c, the coverage evolution during such simulated cathodic scan at different supplied energies is shown. At a high supplied energy of $8k_B T$, the system is able to access almost all coverage states and equilibrate to the GM, giving a very similar as the GM-only and Boltzmann picture assuming global thermodynamic equilibrium. At a lower supplied energy of $1k_B T$, the onset potential of the first row-shifting is postponed slightly, due to kinetic trapping. Note that such postponing is not a simple translation but highly dependent on the local structure of the free energy surface. For example, a new step of 1/2 ML corresponding to

the second row-shifting emerges as -0.28 V_{SHE}, which is a metastable LM with intermediate coverage and not observed in the thermodynamic picture. At even smaller supplied energies, the onset potentials corresponding to restructuring are postponed even more, however, all of them are able to access 1 ML coverage before -0.5 V_{SHE}. The suppression of restructuring at higher pH is not observed, likely because the pH effect within the CHE scheme is addressed by adding a thermodynamic correction term to the μ_H, which leads to simple translation of the curve in Figure 4c without changing its shape.

The failure to capture such restructuring suppression at high pH suggests the presence of another factor which acts against the coverage increase. Here we attribute it to the configurational entropic contribution: The restructuring of Cu to form a protruding row (over some critical initiation length) and the local H-coverage increase to stabilize the row, come with a configurational entropic penalty of the whole interface. Faster intra-surface H diffusion will tend to smear out the local high coverages toward the global average, whereas a faster surface-solution exchange will favor larger fluctuation of local coverages (which can initiate row-shifting). Entropy maximization can be viewed as a phenomenological collective "restoring force", which is the generalized conjugate force of adsorbate coverage (coupled with restructuring events). It opposes ordering and drives the system to a uniform coverage, thus depleting high local coverage needed to initiate restructuring (Schematic S1). The "force" is a collective of many factors and may change as a function of pH and current coverage. Since we are not able to explicitly evaluate such a force with the current model, in Figure 4d we simulate the cathodic scans with $1k_BT$ supplied energy and with different "restoring force constants", $k_{restore}$, to probe the impact of it on the surface phase diagram. At $k_{restore}$=0.1 eV/adsorbate^2, the onset potential for the formation of the 1/6 ML, 1/2 ML, and 1 ML states are postponed to -0.17 -0.36, and -0.42 V_{SHE}, respectively, approaching the experimental results. At $k_{restore}$=1 eV/adsorbate^2, the steps are smoothened due to reshaping of the local free energy surface, the onset potential for 1/6 ML and 1/2 ML states are postponed to -0.23 and -0.41 V_{SHE}, respectively, and the 1 ML state does not form before -0.5 V_{SHE}. At $k_{restore}$=10 eV/adsorbate^2, the entropic restoring potential overrides the flat low-coverage region of the free energy surface, and no row-shifting is observed in the entire potential window of 0 to -0.5 V_{SHE}. Considering the competition with HER at more negative potentials, the restructuring may be completely prevented.

We note that the above analysis is purely phenomenological and provides not a proof of a mechanism but a possible insight: the restructuring events could involve local barriers in the free energy surface, which render the thermodynamic-based statistics problematic. The entropic contributions in the surface restructuring process are crucial for understanding the experimental surface measurements. The results call for going beyond

the global accessibility assumption and incorporating entropic effects for describing the restructuring surfaces.

The proposed model of reconstruction under high coverage of H, and the interplay between H migration and row-shifting is supported by Born-Oppenheimer molecular dynamics (BOMD) simulations, performed for unrestructured surface at 1/36 ML and 1/6 ML coverage, and the shifted-row surface at 1/6 ML coverage, in the NVT ensemble at 300 K with Nosé–Hoover thermostat (Figures

At 1/6 ML H, the mobility of H remains high on unreconstructed surface, though apparently slightly hindered by H-H interaction. No spontaneous reconstruction of Cu is observed for 1/36 ML and 1/6 ML coverage, within the simulated timescale of 10 ps. However, if the BOMD of 1/6 ML coverage starts from a shifted-row GM configuration, H atoms stays in the vicinity of the shifted row, hopping between 3-fold hollow sites in time scale of c.a. 1 ps. No H migration into the unrestructured region is observed. This sharp contrast of H migration kinetics before and after row-shifting is confirmed by CINEB calculations (Figure S14): H-migration on unrestructured Cu(100) is nearly barrier-less, migration along the shifted row has a significant barrier of 0.10 eV, and migration away from the shifted row to the 4-fold hollow site on the unrestructured surface is more hindered with a barrier of 0.28 eV and ΔG of 0.25 eV. In other words, the shifted row acts as a local H trap. The results help interpreting the blurry STM image at the start of the stripe formation: the shifted row is partially occupied then, with frequent H hopping between 3-fold hollow sites along the stripe.

Lastly, row-shifting does not spontaneously occur in BOMD starting from unreconstructed Cu surface at 1/36 and 1/6 ML, in 10 ps, but at 1/3 ML on the unrestructured surface (Figures 5e, S13), spontaneous Cu row-shifting is directly observed in the dynamics. Notably, the H migration creates local regions of higher surface concentration of H, weakening Cu_{top}-Cu_{sub}, and causing transient row intrusions. However, a sufficient local concentration of H is required to stabilize such intrusions, otherwise hydrogens would dissipate and return the surface to the pristine configuration. We compare the RMSD of the top-layer Cu atoms during all BOMD simulations in Figure 5e, to illustrate these local coverage-dependent effects. The coverage dependence of surface dynamics and coordination environments are detailed in Supplementary Note 2. Accordingly, CINEB shows the Cu row-shifting to be highly endothermic and kinetically unfeasible without H on the surface, but exothermic and kinetically feasible at increased coverage, and barriers-less at 1/3 ML, resulting from the strong H binding at 3-fold hollow sites (Figure S16 and Supplementary Note S1). Taken together, these results illustrate how the serendipitous

creation of local high concentration of H is essential for successful and sustained Cu reconstruction, despite the thermodynamic drive toward it. This supports the kinetic and entropic arguments for the delay of Cu reconstruction as a function of the electrode potential in the experiment (Figure 4), overriding the thermodynamics-based prediction.

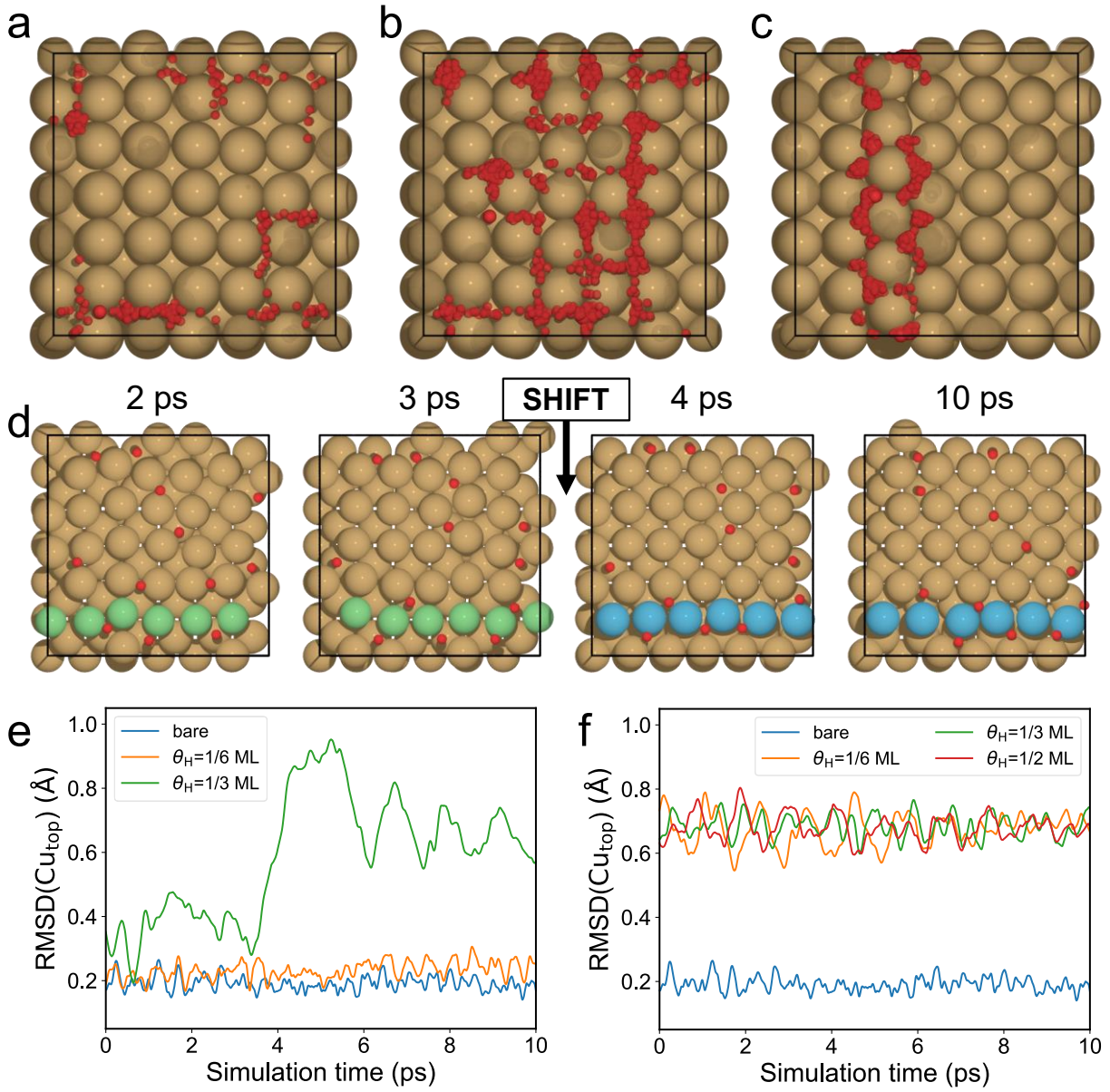

Figure 5. Dynamics of H-covered Cu(100) with different initial configurations and H coverage. The spatial distribution of surface atoms on (a) 1H-covered, (b) unrestructured 6H-covered, and (c) shifted-row 6H-covered Cu(100) surfaces during equilibrated BOMD simulations of 10 ps duration. (d) Key snapshots during an equilibrated 10-ps BOMD simulation of 12H state with an

unrestructured initial configuration (the shifting row is highlighted by green or blue, before or after the shift). RMSD of top-layer Cu positions during equilibrated 10-ps BOMD simulations of ∈ unrestructured surface with 0, 1/6, 1/3 ML H coverage and (f) shifted-row surface with 1/6, 1/3, a½1/2 ML H coverages.

CONCLUSIONS

This work extensively explores the chemical space of H-covered Cu(100) (with adsorbate coverage/configuration and electrochemical potential explicitly addressed) and provides atomistic insight into the hydrogen-induced stripe-restructuring of Cu(100) in electrochemical conditions. We discover a Cu shifted-row restructuring pattern which forms upon H adsorption at a negative electrode potential. The simulated STM images of the predicted phases agree with and rationalize the structural patterns in experimental *in situ* STM spectra including blurry stripes, bright stripe of different surface density, inter-stripe dark lines, and bright spots along the dark lines seen at various potentials. Chemical bonding analysis reveals the weakening of Cu-Cu bond between the top- and sub-layer by the H adsorbates, which facilitates the row-shifting both kinetically and thermodynamically. The row-shifting creates 3-fold hollow sites with high H affinity, which acts as local H trap and stabilizes the restructuring stripe upon H coverage, ultimately leading to a hydride-like surface phase. Row-shifting is observed in BOMD simulation at 1/3 ML H coverage in time scale of a few picoseconds at room temperature, and analysis indicates enhanced Cu mobility and reduced H mobility as H coverage increases. Different statistical models for describing the potential- and pH-dependence of the surface phase are discussed, and the discrepancies from experiments are probed with these models. We show how metastability domains can significantly hinder the restructuring to a more negative onset potential and reveal the surface phases with intermediate coverages. Limitation of the existing thermodynamic-based model for predicting surface phase and pH dependence are discussed, and possible direction for revision are proposed, which include entropic and kinetic effects. We believe the gained insights allows deeper understanding and potential utilization of the surface restructuring in electrocatalysts and functional materials.

METHODS

1. Model Set-up

The Cu(100) surface is modeled by a 4-layer 6×6 supercell of Cu(100) termination with a cell dimension of 15.336 Å×15.336 Å (constructed with experimental lattice parameter from ref [25]). The bottom two layers of the slab are constrained as bulk region, and everything else are allowed to relax as the interface region. A vacuum slab of 15 Å thickness is added in Z direction to avoid spurious interactions between periodic images.

2. DFT calculations

The local optimizations and energy evaluation are performed with the RPBE functional[26] and PBE_PAW pseudopotentials[27] using the VASP program (version 5.4.4).[28–31] The convergence criteria for electronic and force minimization are set to 10^{-5} eV and 0.05 eV/Å during the global optimization and 10^{-6} eV and 0.01 eV/Å for the final refinement. Due to the relatively large system and sampling size, only the Γ *k*-point is sampled in the reciprocal space of the Brillouin zone throughout, and the cutoff energy for the kinetic energy of the plane-waves was 400 eV.

The transition states (TS) are located using climbing image nudged elastic band (CI-NEB) method[32] with image dependent pair potential (IDPP) interpolation.[33] Each TS geometry has been confirmed to have only one imaginary mode.

All electronic structure analyses are performed based on converged charge density or wavefunction. The Bader charges are calculated using Bader Charge Analysis program.[34] The QTAIM analysis is performed using the critic2 program using the Wigner-Seitz method with a subdivision level of 2.[35] The COHP analysis is performed using LOBSTER program with the pbeVaspFit2015 basis set.[36]

3. STM simulations

STM images are simulated using the BSKAN package[37] based on the converged wavefunction generated by VASP. The vacuum is increased to 30 Å to eliminate the response from the other side of the slab. The Tersoff-Hamman approach is used with a bias voltage of 20 mV, corresponding to the experimental value in ref [14,15]. Constant current scans with a current value of 4 μA are performed to give the simulated STM images.

4. Grand Canonical Genetic Algorithm

To sample the chemical space of both Cu restructuring and H coverage/configuration, we performed global optimization using the grand canonical genetic algorithm (GCGA) as implemented in our open-source GOCIA python package (https://github.com/zishengz/gocia). To be specific, the system is treated as a grand canonical ensemble of H adsorbates, and the search target is to minimize the coverage-dependent grand canonical free energy Ω_{H}:

$$\Omega_{\mathrm{H}} = U - TS - \sum \mu N \approx E^{\mathrm{slab}-n\mathrm{H}} - E^{\mathrm{slab}} - n \cdot \mu_{\mathrm{H}}(\mathrm{pH}, U, T) \quad (1)$$

Where the $E^{\mathrm{slab}-n\mathrm{H}}$ and E^{slab} are electronic energies of the H-covered and the bare Cu(100) slab. The vibrational contributions to free energy by the slab atoms are neglected considering their small contribution and high computational cost.[38] The chemical potential of H, μ_{H}, is calculated by:

$$\begin{aligned} \mu_{\mathrm{H}}(\mathrm{pH}, U, T) = \tfrac{1}{2} E_{\mathrm{H_2}}^{\mathrm{gas}} - \ln(10)\, k_{\mathrm{B}} T \mathrm{pH} - |e| U_{\mathrm{SHE}} \\ + \left(\mathrm{ZPE}^{\mathrm{gas}} + C_p^{\mathrm{gas}} - TS^{\mathrm{gas}}\right) - \left(\mathrm{ZPE}^{\mathrm{ads}} + C_p^{\mathrm{ads}} - TS^{\mathrm{ads}}\right) \end{aligned} \quad (2)$$

Where the pH and U (in SHE scale) dependent terms are calculated using the computational hydrogen electrode model.[39] The ZPE and thermal contribution terms of adsorbates are obtained from frequency calculations and evaluated at 298.15 K (see Supplementary Note 4 for details).

A population size of 25 and a mutation rate of 30% are chosen for the GCGA sampling. The pool of initial candidates is generated using the bond length distribution algorithm (BLDA) which is a random structure generation method based on the covalent radii of the atoms.[40] A pre-optimization with Hookean potential is performed to produce reasonable starting geometries before they are fed to electronic structure method codes for local optimization and energy evaluation. Mating between the candidates alive to create offspring by the Split-and-splice operation,[41] in which the parent slabs are cut along a random plane and then spliced together. Fitness factor is assigned to each candidate based on the mating counts and the grand canonical free energy. Candidates with higher fitness are more probable to mate. Similarity check against the current population is performed before adding any new candidate to remove duplicates. Adopted mutation operations include: (1) adding or removing an adsorbate, (2) rattling the surface atoms along random vectors drawn from a normal distribution, (3) translating the buffer slab along x or y axis by 1/n (n=2,3,6) of the cell length, (4) permuting a random half of buffer slab. If an offspring is too similar with its parent, its mutation rate is raised to 100%. Upon the addition of each offspring to the population, the candidate with the lowest fitness is archived to maintain the population size. The structures with unbound fragments

are removed from the population to avoid sampling into chemically irrelevant regions of the PES. The progress plot of a typical GCGA search is shown in Figure S21.

5. Grand canonical DFT calculations.

Under a constant applied potential, the electrode surface is effectively a grand canonical ensemble of electrons where the number of electrons is varied to adapt to the change in the workfunction of the surface. The potential-dependent electronic grand canonical free energy of the surface Ω_{el} can be approximated by a surface charging model:[22]

$$\Omega_{\mathrm{el}}(U) = E(U) - q(U) \cdot FU \approx E(U_0) - \frac{1}{2} C (U - U_0)^2 \tag{3}$$

Which treats the electrochemical interface as an effective capacitor. Here, $E(U)$ is the electronic energy of the surface under a potential U which is calculated by refencing the Fermi level of the system against the vacuum level. $q(U)$ is the surface charge difference referenced against the neutral system, and F is the Faradaic constant. U_0 stands for the potential of zero charge in vacuum scale, and C is the effective capacitance.

The self-consistent implicit solvation model VASPsol[42] is used to represent the polarizable electrolyte region. The surface slab is symmetrized along z axis to avoid asymmetric potential in the implicit solvation region. The thickness of implicit solvent slab is increased to 5λ where the Debye screening length is evaluated by:[43]

$$\lambda \approx \frac{3}{\sqrt{I}} \text{Å} \tag{4}$$

Where I is the ionic strength in M, in this study we take it to be 0.1 to model the 0.1 M $HClO_4$. Hence the implicit solvent thickness is set to 50 Å for the symmetrized slab (Figure S1c).

By varying the number of electrons in the system, the $E(U)$ of the system at the corresponding U and $q(U)$ can be obtained, and thereby a quadratic relation between $\Omega_{el}(U)$ and U can be fitted by sampling a series of q values (see Supplementary Note 5 for details). The U (in vacuum scale) can be converted into the SHE scale by referencing it against the benchmarked value (4.60 V for VASPsol).[44]

The final coverage- and potential-dependent grand canonical free energy Ω_{tot} is approximated by:

$$\Omega_{\mathrm{tot}}(n, U) \approx \Omega_{\mathrm{el}}^{\mathrm{slab}-n\mathrm{H}}(U) - \Omega_{\mathrm{el}}^{\mathrm{slab}}(U) - n \cdot \mu_{\mathrm{H}}(\mathrm{pH}, U, T) \tag{5}$$

6. Molecular dynamics.

The ab initio molecular dynamics simulations are performed on the optimized structures with the same DFT setting as the geometry optimization using the VASP program. The simulation is performed in the NVT (canonical) ensemble at 300 K with the Nose-Hoover thermostat. The time step is set to 1 fs, and a 10 ps trajectory after the equilibration of the system is collected for analysis. The radial distribution function analysis is performed using the VMD program (version 1.9.4a48).[45]

ASSOCIATED CONTENT

Supporting Information.

The following files are available free of charge at xxx.

Computational details; simulated STM images; Bader charge of surface atoms; COHP analysis of selected surface states and bulk references; reaction profile of row-shifting and H migration; QTAIM analysis of surface bonds during row-shifting; selected snapshots of BOMD simulations; progress plot of a typical GCGA search; quadratic fit for the GCDFT calculations; discussions on vibrational contribution to the free energy, details of GCDFT calculations, notable structures in previous reports, and symmetric/asymmetric alignment of H along the shifted row.

AUTHOR INFORMATION

Corresponding Author

*Corresponding Author's email:

Anastassia N. Alexandrova: ana@chem.ucla.edu ,

Philippe Sautet: sautet@ucla.edu

Notes

The authors declare no competing financial interest.

ACKNOWLEDGMENTS

The work was supported by the National Science Foundation CBET grant 2103116. Computational resources for this work were provided by UCLA shared cluster Hoffman2, and the Innovative and Novel Computational Impact on Theory and Experiment (INCITE) program at the Argonne Leadership Computing Facility, which is a DOE Office of Science User Facility supported under Contract DE-AC02-06CH11357.

REFERENCES

1. Zhang, Z., Zandkarimi, B. & Alexandrova, A. N. Ensembles of Metastable States Govern Heterogeneous Catalysis on Dynamic Interfaces. *Acc. Chem. Res.* 53, 447–458 (2020).

2. Zhang, Z., Cui, Z.-H., Jimenez-Izal, E., Sautet, P. & Alexandrova, A. N. Hydrogen Evolution on Restructured B-Rich WB: Metastable Surface States and Isolated Active Sites. *ACS Catal.* 10, 13867–13877 (2020).

3. Hofman, M. S., Wang, D. Z., Yang, Y. & Koel, B. E. Interactions of incident H atoms with metal surfaces. *Surf. Sci. Rep.* 73, 153–189 (2018).

4. Nitopi, S. *et al.* Progress and Perspectives of Electrochemical CO2 Reduction on Copper in Aqueous Electrolyte. *Chem. Rev.* 119, 7610–7672 (2019).

5. Zhao, J. *et al.* An overview of Cu-based heterogeneous electrocatalysts for CO 2 reduction. *J. Mater. Chem. A* 8, 4700–4734 (2020).

6. Yu, J. *et al.* Recent progresses in electrochemical carbon dioxide reduction on copper-based catalysts toward multicarbon products. *Adv. Funct. Mater.* 31, 2102151 (2021).

7. Kim, Y.-G., Baricuatro, J. H., Javier, A., Gregoire, J. M. & Soriaga, M. P. The evolution of the polycrystalline copper surface, first to Cu (111) and then to Cu (100), at a fixed CO2RR potential: A study by operando EC-STM. *Langmuir* 30, 15053–15056 (2014).

8. Gunathunge, C. M. *et al.* Spectroscopic observation of reversible surface reconstruction of copper electrodes under CO2 reduction. *J. Phys. Chem. C* 121, 12337–12344 (2017).

9. Weng, Z. *et al.* Active sites of copper-complex catalytic materials for electrochemical carbon dioxide reduction. *Nat. Commun.* 9, 1–9 (2018).

10. Huang, J. *et al.* Potential-induced nanoclustering of metallic catalysts during electrochemical CO2 reduction. *Nat. Commun.* 9, 3117 (2018).

11. Eren, B. *et al.* Activation of Cu (111) surface by decomposition into nanoclusters driven by CO adsorption. *Science (80-.).* 351, 475–478 (2016).

12. Osowiecki, W. T. *et al.* Factors and Dynamics of Cu Nanocrystal Reconstruction under CO2 Reduction. *ACS Appl. Energy Mater.* 2, 7744–7749 (2019).

13. Auer, A. *et al.* Self-activation of copper electrodes during CO electro-oxidation in

alkaline electrolyte. *Nat. Catal.* 3, 797–803 (2020).

14. Matsushima, H., Haak, C., Taranovskyy, A., Gründer, Y. & Magnussen, O. M. In situ video STM studies of the hydrogen-induced reconstruction of Cu (100): potential and pH dependence. *Phys. Chem. Chem. Phys.* 12, 13992–13998 (2010).

15. Matsushima, H., Taranovskyy, A., Haak, C., Gründer, Y. & Magnussen, O. M. Reconstruction of Cu(100) Electrode Surfaces during Hydrogen Evolution. *J. Am. Chem. Soc.* 131, 10362–10363 (2009).

16. Hellman, A., Svensson, K. & Andersson, S. Hydrogen-induced reconstruction of Cu (100): two-dimensional and one-dimensional structures of surface hydride. *J. Phys. Chem. C* 118, 15773–15778 (2014).

17. Duan, Z. & Henkelman, G. Atomic-Scale Mechanisms of Electrochemical Pt Dissolution. *ACS Catal.* 11, 14439–14447 (2021).

18. Tipton, W. W. & Hennig, R. G. A grand canonical genetic algorithm for the prediction of multi-component phase diagrams and testing of empirical potentials. *J. Phys. Condens. Matter* 25, 495401 (2013).

19. Sun, G., Alexandrova, A. N. & Sautet, P. Pt8 cluster on alumina under a pressure of hydrogen: Support-dependent reconstruction from first-principles global optimization. *J. Chem. Phys.* 151, 194703 (2019).

20. Mönig, H. *et al.* Understanding scanning tunneling microscopy contrast mechanisms on metal oxides: a case study. *ACS Nano* 7, 10233–10244 (2013).

21. Tackett, B. M., Raciti, D., Hight Walker, A. R. & Moffat, T. P. Surface Hydride Formation on Cu(111) and Its Decomposition to Form H2 in Acid Electrolytes. *J. Phys. Chem. Lett.* 12, 10936–10941 (2021).

22. Steinmann, S. N., Michel, C., Schwiedernoch, R. & Sautet, P. Impacts of electrode potentials and solvents on the electroreduction of CO 2: a comparison of theoretical approaches. *Phys. Chem. Chem. Phys.* 17, 13949–13963 (2015).

23. Ma, T. & Wang, S. *Phase transition dynamics*. (Springer, 2014).

24. Wu, Z.-Z. *et al.* Identification of Cu(100)/Cu(111) Interfaces as Superior Active Sites for CO Dimerization During CO2 Electroreduction. *J. Am. Chem. Soc.* 144, 259–269 (2022).

25. Janthon, P. *et al.* Bulk Properties of Transition Metals: A Challenge for the Design of Universal Density Functionals. *J. Chem. Theory Comput.* 10, 3832–3839 (2014).

26. Hammer, B., Hansen, L. B. & Nørskov, J. K. Improved adsorption energetics

within density-functional theory using revised Perdew-Burke-Ernzerhof functionals. *Phys. Rev. B* 59, 7413 (1999).

27. Kresse, G. & Joubert, D. From ultrasoft pseudopotentials to the projector augmented-wave method. *Phys. Rev. b* 59, 1758 (1999).

28. Kresse, G. & Furthmüller, J. Efficiency of ab-initio total energy calculations for metals and semiconductors using a plane-wave basis set. *Comput. Mater. Sci.* 6, 15–50 (1996).

29. Kresse, G. & Furthmüller, J. Efficient iterative schemes for ab initio total-energy calculations using a plane-wave basis set. *Phys. Rev. B* 54, 11169–11186 (1996).

30. Kresse, G. & Hafner, J. Ab initio molecular dynamics for liquid metals. *Phys. Rev. B* 47, 558 (1993).

31. Kresse, G. & Hafner, J. Ab initio molecular-dynamics simulation of the liquid-metal–amorphous-semiconductor transition in germanium. *Phys. Rev. B* 49, 14251 (1994).

32. Henkelman, G., Uberuaga, B. P. & Jónsson, H. A climbing image nudged elastic band method for finding saddle points and minimum energy paths. *J. Chem. Phys.* 113, 9901–9904 (2000).

33. Smidstrup, S., Pedersen, A., Stokbro, K. & Jónsson, H. Improved initial guess for minimum energy path calculations. *J. Chem. Phys.* 140, 214106 (2014).

34. Yu, M. & Trinkle, D. R. Accurate and efficient algorithm for Bader charge integration. *J. Chem. Phys.* 134, 64111 (2011).

35. Otero-de-la-Roza, A., Johnson, E. R. & Luaña, V. Critic2: A program for real-space analysis of quantum chemical interactions in solids. *Comput. Phys. Commun.* 185, 1007–1018 (2014).

36. Nelson, R. *et al.* LOBSTER: Local orbital projections, atomic charges, and chemical-bonding analysis from projector-augmented-wave-based density-functional theory. *J. Comput. Chem.* 41, 1931–1940 (2020).

37. Hofer, W. A. A Guide to simulation of STM images and spectra from first principles: bSKAN 3.6. *Surf. Sci. Res. Centre, Univ. Liverpool, Liverpool, UK* 60 (2005).

38. Sun, G., Alexandrova, A. N. & Sautet, P. Structural Rearrangements of Subnanometer Cu Oxide Clusters Govern Catalytic Oxidation. *ACS Catal.* 10, 5309–5317 (2020).

39. Nørskov, J. K. *et al.* Trends in the exchange current for hydrogen evolution. *J.*

Electrochem. Soc. 152, J23–J26 (2005).

40. Zhai, H. & Alexandrova, A. N. Ensemble-Average Representation of Pt Clusters in Conditions of Catalysis Accessed through GPU Accelerated Deep Neural Network Fitting Global Optimization. *J. Chem. Theory Comput.* 12, 6213–6226 (2016).

41. Deaven, D. M. & Ho, K.-M. Molecular geometry optimization with a genetic algorithm. *Phys. Rev. Lett.* 75, 288 (1995).

42. Mathew, K., Sundararaman, R., Letchworth-Weaver, K., Arias, T. A. & Hennig, R. G. Implicit solvation model for density-functional study of nanocrystal surfaces and reaction pathways. *J. Chem. Phys.* 140, 84106 (2014).

43. Steinmann, S. N. & Sautet, P. Assessing a First-Principles Model of an Electrochemical Interface by Comparison with Experiment. *J. Phys. Chem. C* 120, 5619–5623 (2016).

44. Mathew, K., Kolluru, V. S. C., Mula, S., Steinmann, S. N. & Hennig, R. G. Implicit self-consistent electrolyte model in plane-wave density-functional theory. *J. Chem. Phys.* 151, 234101 (2019).

45. Humphrey, W., Dalke, A. & Schulten, K. VMD: visual molecular dynamics. *J. Mol. Graph.* 14, 33–38 (1996).